*1998 IEEE Nuclear Science Symposium and Medical Imaging Conference Record,* pages 1953–1958 (preprint)

# Kinetic Parameter Estimation from Dynamic Cardiac Patient SPECT Projection Measurements[1]

BW Reutter[†], *Member, IEEE*; GT Gullberg[‡], *Senior Member, IEEE*;
and RH Huesman[†], *Senior Member, IEEE*
[†]Center for Functional Imaging, Lawrence Berkeley National Laboratory
University of California, Berkeley, CA 94720, USA
[‡]Department of Radiology, University of Utah, Salt Lake City, UT 84132, USA

## *Abstract*

The estimation of kinetic parameters directly from projection data is potentially useful for clinical dynamic cardiac SPECT studies, particularly those using a single detector system or body contouring orbits with a multi-detector system. A dynamic image sequence reconstructed from the inconsistent projections acquired by a relatively slowly rotating gantry can contain artifacts that lead to biases in kinetic parameters estimated from time-activity curves generated by overlaying regions of interest on the images. Using simulated data we have shown that unbiased kinetic parameter estimates can be obtained directly from the projections.

Here we present results of a $^{99m}$Tc-teboroxime patient study where the regions of the left ventricular myocardium, blood pool, liver, and background tissue were determined by automatically segmenting a dynamic image sequence reconstructed from the inconsistent projection data. A spatial model for the projections was then created and one compartment kinetic model parameters for the myocardium and liver were estimated directly from the projections.

## I. Introduction

Conventional analysis of dynamically acquired nuclear medicine data involves fitting kinetic models to time-activity curves generated by overlaying regions of interest on a temporal sequence of reconstructed images. Since dynamic single photon emission computed tomography (SPECT) data acquisition involves gantry motion and the distribution of radiopharmaceutical changes during the acquisition, projections at different angles come from different tracer distributions. Images reconstructed from these inconsistent projections can contain artifacts that lead to biases in the estimated kinetic parameters.

To overcome this problem we have been investigating the estimation of kinetic parameters directly from projection data by modeling the spatial and temporal distribution of the radiopharmaceutical within the SPECT field of view. Using simulated data we have shown that unbiased kinetic parameter estimates can be obtained directly from the projections [1, 2].

This approach is potentially useful for clinical studies, particularly in those clinics which have only single detector SPECT systems and thus are not able to perform rapid tomographic acquisitions. Even with a three-detector system, a patient study that utilizes body contouring orbits can take 45–60 sec to obtain one full tomographic acquisition. Thus, the estimation of kinetic parameters directly from projection data may be useful for multi-detector SPECT systems in some cases.

Here we present results of a $^{99m}$Tc-teboroxime patient study where the regions of the left ventricular myocardium, blood pool, liver, and background tissue were determined by automatically segmenting a dynamic image sequence reconstructed from the inconsistent projection data. A spatial model for the projections was then created and one compartment kinetic model parameters for the myocardium and liver were estimated directly from the projections.

## II. Data Acquisition

A dynamic cardiac patient SPECT study was performed at the University of Utah Medical Center. Data were acquired using a Picker PRISM 3000XP three-detector SPECT system. First, a transmission scan was performed: 65 cm focal length fan-beam collimators were mounted to each detector and 120 transmission projections of 64×64 images were acquired over 360° using a $^{153}$Gd line source as the transmission source. Then, the fan-beam collimators were replaced with parallel collimators for the dynamic cardiac SPECT study. Vasodilation was induced pharmacologically using adenosine. A 15 min dynamic acquisition obtaining 120 projections over 360° every 10 sec was initiated at the same time as the injection of 25 mCi of $^{99m}$Tc-teboroxime. About 4.8 million emission events were acquired.

## III. Automated Volume of Interest Specification

The attenuation map was reconstructed from the truncated transmission data using 20 iterations of the transmission iterative ML-EM algorithm. The transmission data were registered to the emission data with the aid of three radioactive markers placed externally around the thorax. Dynamic emission images with attenuation correction were reconstructed using 20 iterations of the iterative ML-EM algorithm. Each of the 90 ten-second frames was composed of 18 contiguous 7.12 mm-thick transverse images. Each transverse image was 64×64 pixels, with pixel size 7.12×7.12 mm.

[1]This work was supported by U.S. Department of Health and Human Services grants R01-HL50663 and P01-HL25840, and by U.S. Department of Energy contract DE-AC03-76SF00098.

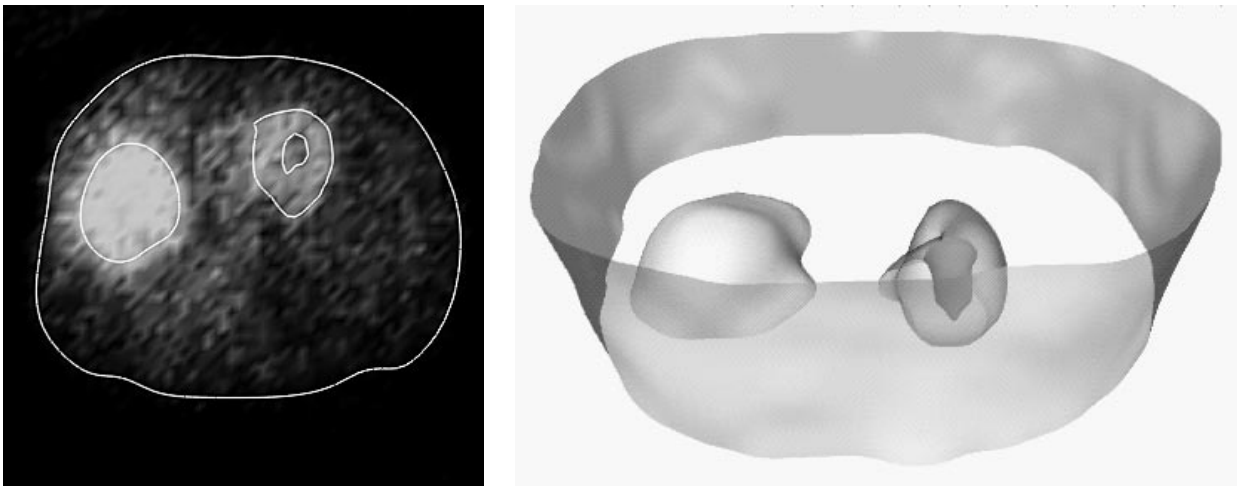

Figure 1: (Left) Contours obtained by taking a transverse cross section through automatically extracted body, liver, and left ventricular surfaces are overlaid upon the corresponding image in the temporally smoothed dataset. (Right) Anterior view of the surfaces, with semi-transparent body and left ventricle. Volume elements lying inside the left ventricular endocardium were used as the blood pool.

The left ventricular myocardium and the liver were enhanced by first temporally smoothing the 64×64×18×90 emission image dataset with a spline approximation [3] to a Gaussian filter having a standard deviation $\sigma_t = 1.2$ time frames (support 1×1×1×7 pixels along the $x$, $y$, $z$, and $t$ axes, respectively). A 3×3×3×1 gray-scale morphological opening operator [4] was then applied to reduce small-scale noise structures, while preserving intensity transitions associated with myocardial and liver uptake.

The background activity in the body was enhanced by first subtracting the temporally smoothed image dataset from the original image dataset and taking the absolute value. To obtain a more uniform background, each resulting pixel was then normalized by the square root of its value in the temporally smoothed dataset and a 3×3×3×1 gray-scale morphological closing operator [4] was applied to fill in small-scale low intensity regions.

The enhanced 64×64×18×90 image datasets were then processed using the 4-D version of an edge detection operator which we have used previously to segment body and lung surfaces automatically in respiratory gated PET transmission images [5, 6]. The edge detection operator estimates the second derivative in the direction of the 4-D image intensity gradient, weighted by the gradient magnitude squared:

$$\|\nabla f\|^2 \left[ \frac{\nabla f}{\|\nabla f\|} \cdot \nabla \left[ \frac{\nabla f}{\|\nabla f\|} \cdot \nabla f \right] \right] = \sum_{p=1}^{4} \sum_{q=1}^{4} \frac{\partial f}{\partial (x^p)} \frac{\partial f}{\partial (x^q)} \frac{\partial^2 f}{\partial (x^p) \partial (x^q)}, \quad (1)$$

where $x^1$, $x^2$, and $x^3$ denote the spatial coordinates and $x^4$ denotes the temporal coordinate. Zero-crossing points in the second directional derivative correspond to local extrema in the image intensity gradient magnitude. Among these are the points that lie on the boundaries or edges between relatively homogeneous regions delineated with adequate contrast.

The first and second order partial derivatives needed to calculate equation (1) were estimated by convolving the images with spline approximations [3] to Gaussian derivative filter kernels that smooth the images prior to performing differentiation. The enhanced myocardium/liver image dataset was processed using kernels with support 7×7×7×31 ($\sigma_x = \sigma_y = \sigma_z = 1.2$ pixels, $\sigma_t = 4.6$ time frames). The enhanced background image dataset was processed using kernels with support 15×15×15×31 ($\sigma_x = \sigma_y = \sigma_z = 2.3$ pixels, $\sigma_t = 4.6$ time frames).

After discarding the results from the first and last two transverse sections, which contained artifacts due to the boundary effects of the image processing, potentially interesting anatomical surfaces were constructed automatically by linking together the zero-crossing points in the second directional derivative operator output at time frame 31, corresponding to 5 min post-injection. Figure 1 shows the body, liver, and left ventricular surfaces extracted automatically from the dynamic SPECT image dataset at time frame 31. Volume elements lying inside the left ventricular endocardium were used as the blood pool. The segmentation took about 8 min on a 150 MHz MIPS R10000-based Silicon Graphics O2 workstation.

## IV. Estimation of Kinetic Parameters Directly from Projections

We formulate a nonlinear estimation problem using a spatial and temporal parametrization of the time-varying distribution measured with a rotating gantry SPECT system. The one compartment model shown in Figure 2 is assumed for myocardial and liver tissue with a known blood input function, which would correspond to the kinetics of teboroxime [7, 8, 9]. Parameters are estimated by minimizing a weighted sum of squared differences between the projections and the model

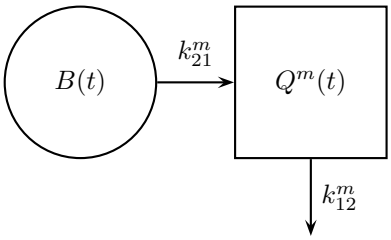


Figure 2: Compartmental model for $^{99m}$Tc-teboroxime in the myocardium.

predicted values.

The expression for activity in tissue type $m$ is

$$\begin{aligned} Q^m(t) &= Q_0^m e^{-k_{12}^m t} + k_{21}^m \int_0^t B(\tau) e^{-k_{12}^m (t-\tau)} d\tau \\ &= Q_0^m U^m(t) + k_{21}^m V^m(t), \end{aligned} \tag{2}$$

where $Q_0^m$ is the initial activity due to a prior injection (if any), $B(t)$ is the blood input function, $k_{21}^m$ is the uptake parameter, and $k_{12}^m$ is the washout parameter. Tissue type 1 is the left ventricular myocardium and tissue type 2 is the liver. Total activity in the tissue is given by

$$\begin{aligned} Q^m(t) + f_v^m B(t) = \\ Q_0^m U^m(t) + k_{21}^m V^m(t) + f_v^m B(t), \end{aligned} \tag{3}$$

where $f_v^m$ is the fraction of vasculature in the tissue.

Using the automatically segmented volumes of interest and the reconstructed attenuation map, the attenuated unit activity projections of each volume were calculated for each projection ray of each projection angle. That is, the number of events that would be detected from each volume, given a static unit concentration of activity within the volume, was calculated for each projection ray of each projection angle. The number of projection rays analyzed per projection angle was $N = 704$ (64 transverse $\times$ 11 axial), the number of projection angles per 360° dataset was $J = 120$, and the number of 360° projection datasets was $I = 90$. Thus, there was a total of about 7.6 million projection rays distributed in space and time.

For the ray at angle $j$ and position $n$, the attenuated unit activity projections of the blood pool, body background, and tissue type $m$ are denoted by $u_{jn}$, $v_{jn}$, and $w_{jn}^m$, respectively. The body background activity function is denoted by $G(t)$ and is assumed to underlie the blood pool and tissue volumes. The projection equations can be expressed as

$$\begin{aligned} p_{ijn} = \int_{t_{ij}-\Delta t}^{t_{ij}} \Bigg\{ & u_{jn} B(\tau) + v_{jn} G(\tau) \\ + \sum_{m=1}^{2} w_{jn}^m & \left[ Q_0^m U^m(\tau) + k_{21}^m V^m(\tau) + f_v^m B(\tau) \right] \Bigg\} d\tau, \end{aligned} \tag{4}$$

where $t_{ij}$ is the time at which the acquisition of $p_{ijn}$ ends and $\Delta t = 0.25$ sec (10 sec per 40 gantry locations). The constants $u_{jn}$, $v_{jn}$, and $w_{jn}^m$ are pure geometrical weighting factors, and the projection equations are linear in the unknowns $Q_0^m$, $k_{21}^m$, and $f_v^m$. The nonlinear parameters $k_{12}^m$ are contained in $U^m(t)$ and $V^m(t)$.

Samples of the blood input and background time-activity curves were estimated directly from the projections using the automatically segmented volumes of interest and the method proposed by Formiconi [10]. These tomographically determined curves were not substituted directly into equation (4), as this appeared to bias the kinetic parameter estimates. Rather, the blood input $B(t)$ and the background $G(t)$ were assumed to have the shapes of these curves, and the amplitudes of these curves were estimated along with the kinetic parameters. Rewriting equation (4) in terms of the shapes and the amplitudes of these curves, one obtains

$$\begin{aligned} p_{ijn} = \int_{t_{ij}-\Delta t}^{t_{ij}} \Bigg\{ & u_{jn} b B'(\tau) + v_{jn} g G'(\tau) \\ + \sum_{m=1}^{2} w_{jn}^m & \left[ Q_0^m U^m(\tau) + k'^m_{21} V'^m(\tau) + f'^m_v B'(\tau) \right] \Bigg\} d\tau, \end{aligned} \tag{5}$$

where $B'(t)$ and $G'(t)$ are the tomographically determined shapes of the blood input and background time-activity curves, $b$ and $g$ are their amplitudes, $V'^m(t) = V^m(t)/b$, $k'^m_{21} = b k_{21}^m$, and $f'^m_v = b f_v^m$. These projection equations are linear in the unknowns $Q_0^m$, $k'^m_{21}$, $f'^m_v$, $b$, and $g$. The nonlinear parameters $k_{12}^m$ are contained in $U^m(t)$ and $V'^m(t)$.

The criterion which was minimized by varying the model parameters is the weighted sum of squares function

$$\chi^2 = \sum_{i=1}^{I} \sum_{j=1}^{J} \sum_{n=1}^{N} \frac{(p_{ijn}^* - p_{ijn})^2}{W_{ijn}}, \tag{6}$$

where $p_{ijn}^*$ are the measured projections and $W_{ijn}$ are weighting factors. The weighting factors were either unity for an unweighted fit, or the estimated variances of the projections for a weighted fit. Given $B'(t)$, $G'(t)$, and values for the nonlinear washout parameters

$$\boldsymbol{\lambda} = \begin{bmatrix} k_{12}^1 & k_{12}^2 \end{bmatrix}, \tag{7}$$

the values of the linear parameters

$$\boldsymbol{\mu} = \begin{bmatrix} Q_0^1 & Q_0^2 & k'^1_{21} & k'^2_{21} & f'^1_v & f'^2_v & b & g \end{bmatrix} \tag{8}$$

which minimize the criterion $\chi^2$ can be estimated using linear least squares. Thus, $\chi^2$ can be expressed as a function of only the nonlinear washout parameter vector $\boldsymbol{\lambda}$ [2].

A modified iterative Newton-Raphson optimization algorithm [11, 12] was used to obtain an estimate $\hat{\boldsymbol{\lambda}}$ of the nonlinear parameter vector. Given $\hat{\boldsymbol{\lambda}}$, an estimate $\hat{\boldsymbol{\mu}}$ of the linear parameter vector was obtained using linear least squares. Estimates of the uptake parameters $\hat{k}_{21}^m$ and the vascular fractions $\hat{f}_v^m$ were obtained as $\hat{k}'^m_{21}/\hat{b}$ and $\hat{f}'^m_v/\hat{b}$, respectively.

An estimate of the covariance matrix of the parameter values $\hat{\boldsymbol{\lambda}}$, $\hat{\boldsymbol{\mu}}$ was obtained by propagating estimates of the variances of the measured projections through a linear least squares approximation to the nonlinear least squares problem [2]. The variances of the uptake parameters $\hat{k}_{21}^m$ and the vascular fractions $\hat{f}_v^m$ were then estimated as follows [13]:

$$\frac{\text{var}(\hat{k}_{21}^m)}{(\hat{k}_{21}^m)^2} = \frac{\text{var}(\hat{k'}_{21}^m)}{(\hat{k'}_{21}^m)^2} + \frac{\text{var}(\hat{b})}{\hat{b}^2} - \frac{2\text{cov}(\hat{k'}_{21}^m, \hat{b})}{\hat{k'}_{21}^m \hat{b}} \quad (9)$$

$$\frac{\text{var}(\hat{f}_v^m)}{(\hat{f}_v^m)^2} = \frac{\text{var}(\hat{f'}_v^m)}{(\hat{f'}_v^m)^2} + \frac{\text{var}(\hat{b})}{\hat{b}^2} - \frac{2\text{cov}(\hat{f'}_v^m, \hat{b})}{\hat{f'}_v^m \hat{b}}. \quad (10)$$

## V. Results

The results of estimating kinetic parameters by minimizing the sum of squares function in equation 6 with and without weighting are given in Table 1.

Column a shows the results obtained for the unweighted case. Starting with the nonlinear washout parameters $\boldsymbol{\lambda}$ at zero, it took seven iterations of the modified Newton-Raphson optimization algorithm to minimize equation (6) with the weights $W_{ijn}$ set to unity. Running on a Cray J90 at the National Energy Research Scientific Computing (NERSC) Center, this took about 1.2 min per iteration.

Column b shows the results obtained for the weighted case. The weights $W_{ijn}$ in equation (6) were determined as follows. Ten iterations of Formiconi's weighted least squares method [10] were used to estimate time-activity curves for all of the segmented volumes directly from the projections. Starting with the weights at unity, an initial set of time-activity curves was estimated. The projections resulting from the initial set of curves were then used as the weights and a second set of curves was estimated. By the third iteration, the sum of squared changes in the projections was less than one; by the tenth iteration, the sum of squared changes was less than $10^{-18}$. The projections obtained after the tenth iteration were used as the weights $W_{ijn}$ in equation (6). Then, starting with the nonlinear washout parameters $\boldsymbol{\lambda}$ at the values obtained from the unweighted fit, it took seven iterations of the modified Newton-Raphson optimization algorithm to minimize equation (6). The same solution was obtained in eight iterations when starting with $\boldsymbol{\lambda}$ at zero. Running on a Cray J90 at the National Energy Research Scientific Computing (NERSC) Center, this took about 5.4 min per iteration.

| | | (a) unweighted fit | (b) weighted fit |
|---|---|---|---|
| myocardium | $k_{21}^1$ | 0.835 ± 0.055 | 0.905 ± 0.063 |
| | $k_{12}^1$ | 0.178 ± 0.002 | 0.142 ± 0.001 |
| | $f_v^1$ | 0.293 ± 0.025 | 0.346 ± 0.030 |
| | $Q_0^1$ | 26.7 ± 0.6 | 20.5 ± 0.5 |
| liver | $k_{21}^2$ | 1.248 ± 0.082 | 1.445 ± 0.100 |
| | $k_{12}^2$ | 0.019 ± 0.0005 | 0.008 ± 0.0004 |
| | $f_v^2$ | -0.057 ± 0.012 | -0.078 ± 0.013 |
| | $Q_0^2$ | 61.6 ± 0.5 | 66.3 ± 0.5 |
| blood | $b$ | 0.999 ± 0.065 | 0.973 ± 0.067 |
| background | $g$ | 1.002 ± 0.0007 | 1.002 ± 0.0006 |

Table 1

Results of estimating kinetic parameters directly from projections acquired for a $^{99m}$Tc-teboroxime patient study. The estimated values are shown along with their estimated uncertainties (standard deviations indicated by ±). Units for uptake $k_{21}^m$ and washout $k_{12}^m$ are min$^{-1}$. Units for initial activity $Q_0^m$ are counts/sec/25cc. The vascular fraction $f_v^m$, blood amplitude $b$, and background amplitude $g$ are dimensionless.

Based on the estimated uncertainties (standard deviations) for the parameter values, the unweighted and weighted fits appeared to yield comparable values for the myocardial uptake parameter $k_{21}^1$. Compared to the unweighted fit, the weighted fit appeared to yield a larger value for the liver uptake parameter $k_{21}^2$, and smaller values for the washout parameters $k_{12}^1$ and $k_{12}^2$. The weighted fit appeared to yield slightly less precise estimates for the uptake parameters and slightly more precise estimates for the washout parameters. The estimated uncertainty for the myocardial uptake was about 7%, for both the unweighted and the weighted fit. The estimated uncertainty for the myocardial washout was about 1%, for both the unweighted and the weighted fit.

Figure 3 shows the time-activity curves obtained by using Formiconi's method and direct kinetic parameter estimation, as well as by conventional overlaying of cross sections of the segmented volumes of interest on the dynamic image reconstructions. The direct methods yielded better separation of the activities in the volumes, compared to the conventional method.

## VI. Summary

The estimation of kinetic parameters directly from projection data is potentially useful for clinical dynamic cardiac SPECT studies, particularly those using a single detector system or body contouring orbits with a multi-detector system. Implementation of this strategy requires a spatial and temporal model of the distribution of radiopharmaceutical within the SPECT field of view. This strategy was used to analyze data from a $^{99m}$Tc-teboroxime patient study.

Automated volume of interest specification based on 4-D edge detection applied to the dynamic image sequence appeared to work well, and will facilitate routine application of direct kinetic parameter estimation. Multiple local minima were not encountered when directly estimating parameters with a weighted fit in which modeled projections obtained with Formiconi's method [10] were used as the weights. Unweighted and weighted direct fits appeared to yield comparable values for myocardial uptake. The weighted fit appeared to yield a slightly less precise estimate, however.

Future work in this area includes incorporating additional physical factors such as scatter and geometric point response in the modeling, validating the volume of interest segmentation algorithm, parametrizing nonuniform activity concentrations within the segmented volumes, fitting better temporal models to the blood input and background activity functions, and

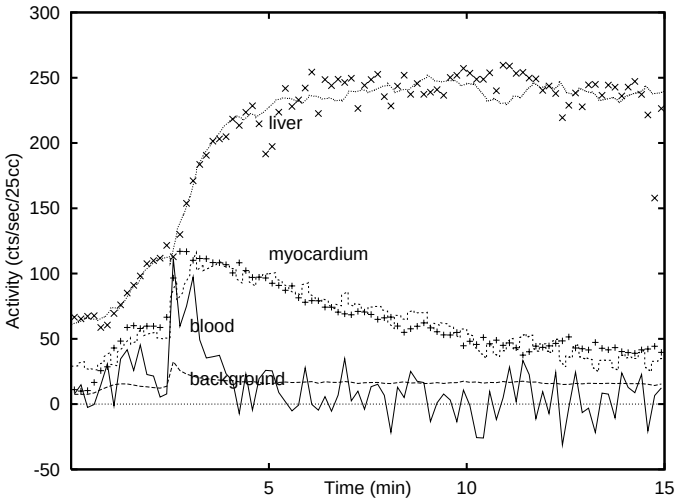


(a) unweighted Formiconi/direct

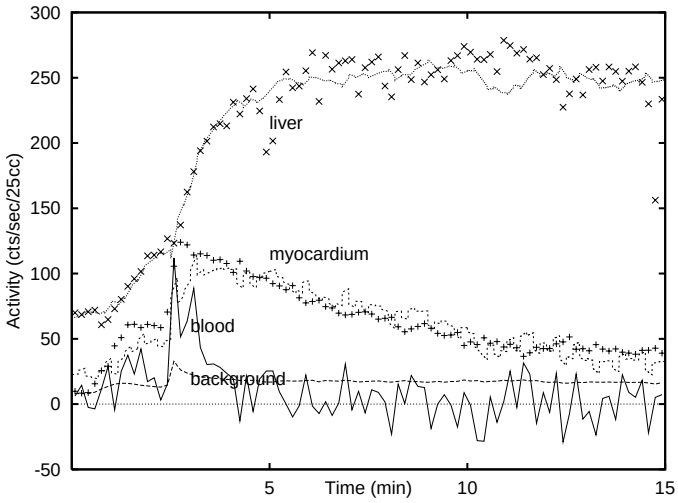


(b) weighted Formiconi/direct

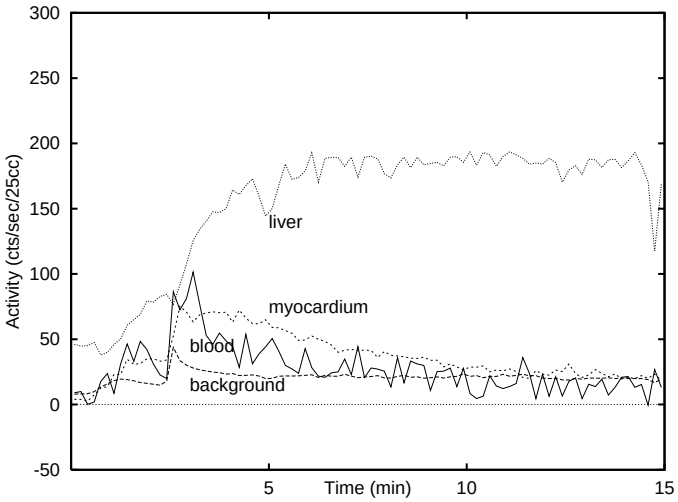


(c) conventional

Figure 3: Time-activity curves obtained by (a) unweighted and (b) weighted estimation directly from the projections, and by (c) overlaying cross sections of the segmented volumes of interest on the dynamic image reconstructions. In (a) and (b), the blood and background curves were obtained using Formiconi's method [10], and the myocardium and liver curves were obtained using direct kinetic parameter estimation. In (a) and (b), there appears to be good agreement between the myocardium and liver curves and the points denoted by $(+)$ and $(\times)$, which were obtained using Formiconi's method. The direct methods yielded better separation of the activities in the volumes, compared to the conventional method.

investigating other methods for performing weighted fits to obtain more precise kinetic parameter estimates.

## VII. Acknowledgments

We thank Dr. EVR Di Bella for his assistance with the data analysis.

This work was supported in part by the National Heart, Lung, and Blood Institute of the U.S. Department of Health and Human Services under grants R01-HL50663 and P01-HL25840; and, in part by the Director, Office of Energy Research, Office of Biological and Environmental Research, Medical Applications and Biophysical Research Division of the U.S. Department of Energy under contract DE-AC03-76SF00098.

This work was developed in part using the computational resources at the National Energy Research Scientific Computing (NERSC) Center at Lawrence Berkeley National Laboratory.

## VIII. References

[1] R H Huesman, B W Reutter, G L Zeng, and G T Gullberg. Kinetic parameter estimation from SPECT cone-beam projection measurements. *Phys Med Biol*, 43(4):973–982, 1998.

[2] B W Reutter, G T Gullberg, and R H Huesman. Kinetic parameter estimation from attenuated SPECT projection measurements. *IEEE Trans Nucl Sci*, in press.

[3] M Unser, A Aldroubi, and M Eden. The $L_2$ polynomial spline pyramid. *IEEE Trans Patt Anal Machine Intell*, 15(4):364–379, 1993.

[4] S R Sternberg. Grayscale morphology. *Comput Vis Graph Imag Proc*, 35(3):333–355, 1986.

[5] B W Reutter, G J Klein, and R H Huesman. Automated 3-D segmentation of respiratory-gated PET transmission images. *IEEE Trans Nucl Sci*, 44(6), 1997.

[6] B W Reutter, G J Klein, and R H Huesman. Respiration-compensated cardiac PET attenuation correction via automated 4-D segmentation of gated transmission

images. *J Nucl Med*, 38(5 suppl):203P, 1997. (abstract).

[7] R K Narra, T Feld, and A D Nunn. Absorbed radiation dose to humans from technetium-99m-teboroxime. *J Nucl Med*, 33(1):88–93, 1992.

[8] A M Smith, G T Gullberg, P E Christian, and F L Datz. Kinetic modeling of teboroxime using dynamic SPECT imaging of a canine model. *J Nucl Med*, 35(3):984–995, 1994.

[9] A M Smith, G T Gullberg, and P E Christian. Experimental verification of $^{99m}$Tc-teboroxime kinetic parameters in the myocardium using dynamic SPECT: Reproducibility, correlations to flow, and susceptibility to extravascular contamination. *J Nucl Cardiol*, 3:130–142, 1996.

[10] A R Formiconi. Least squares algorithm for region-of-interest evaluation in emission tomography. *IEEE Trans Med Imag*, 12(1):90–100, 1993.

[11] D M Bates and D G Watts. *Nonlinear Regression Analysis and Its Applications*. John Wiley & Sons, New York, 1988.

[12] G A F Seber and C J Wild. *Nonlinear Regression*. John Wiley & Sons, New York, 1989.

[13] M Kendall, A Stuart, and J K Ord. *Kendall's Advanced Theory of Statistics*, volume 1, sections 10.5–10.6. Oxford University Press, New York, 1987.

## DISCLAIMER

This document was prepared as an account of work sponsored by the United States Government. While this document is believed to contain correct information, neither the United States Government nor any agency thereof, nor The Regents of the University of California, nor any of their employees, makes any warranty, express or implied, or assumes any legal responsibility for the accuracy, completeness, or usefulness of any information, apparatus, product, or process disclosed, or represents that its use would not infringe privately owned rights. Reference herein to any specific commercial product, process, or service by its trade name, trademark, manufacturer, or otherwise, does not necessarily constitute or imply its endorsement, recommendation, or favoring by the United States Government or any agency thereof, or The Regents of the University of California. The views and opinions of authors expressed herein do not necessarily state or reflect those of the United States Government or any agency thereof, or The Regents of the University of California.

Ernest Orlando Lawrence Berkeley National Laboratory is an equal opportunity employer.